
Article:
Zhang, R. and Smith, C.C. orcid.org/0000-0002-0611-9227 (2020) Upper bound limit analysis of soils with a non-linear failure criterion. Canadian Geotechnical Journal, 57 (3). pp. 423-432. ISSN 0008-3674

https://doi.org/10.1139/cgj-2018-0513

Upper Bound Limit Analysis of Soils With a Non-linear Failure Criterion

Rui, Z. and Smith, C.C.

Abstract: Limit analysis is a widely used technique for the analysis of geotechnical collapse states and there exists a significant body of literature covering its application to soils with a linear failure criterion. However, such a failure criterion is often an idealisation of an actual non-linear response for which available analytical techniques are limited. This paper presents a new fully general solution procedure for generating upper bound multi-wedge rigid block mechanisms for a soil with a non-linear failure criterion, utilising a curved interface that obeys the non-linear yield function flow rule along its full length. This work extends the long established kinematic sliding wedge approach for linear soils and is illustrated through application to active and passive retaining wall and anchor/trapdoor problems. Through additional consideration of the lower bound solution, close bounds on the retaining wall problem to within $\sim$1% are established. The ability of the non-linear upper bound solution to predict the shear and normal stress at every point along the failure surface is discussed.

Key words: Limit analysis; Nonlinear failure; Upper Bound.

1. Introduction

The prediction of failure mechanisms in geotechnical engineering has many important applications in the design of such structures as retaining walls, foundations, slopes, buried pipes and culverts, ground anchors and silos. Limit analysis is a common approach applied to such problems and the theory has been extensively covered by *e.g.* Chen (1975) and Chen & Liu (1990), primarily for soils following a linear Mohr Coulomb criterion. However, the assumption of linear behaviour of soil is an idealisation and non-linear behaviour can be significant for some soils and fractured rock systems (*e.g.* Baker 2004, Hoek & Brown 1997, Mohammadi & Tavakoli 2015).

While recent work by *e.g.* Ukritchon & Keawsawasvong (2018) has demonstrated the modelling of non-linear behaviour in a finite element limit analysis framework, this paper is concerned with a discrete slip-line kinematic approach, which has application both for hand calculations and as part of a general purpose numerical approach *e.g.* Smith & Gilbert (2007) and Hambleton & Sloan (2013).

Several authors have addressed such a problem. Baker & Frydman (1983) and Chen (1975) described a method for undertaking slope stability analysis for non-linear soils using a variational approach, but which required numerical integration. Soon & Drescher (2007) presented an approach based on the classic multi-wedge rigid block upper bound kinematic method, using straight slip-lines but a specific linear yield surface for each sliding interface, where this linear surface was selected as a tangent to the non-linear yield surface. The specific tangent location was chosen as part of a multivari-

Rui, Z. and Smith, C.C..[1] University of Sheffield, Department of Civil and Structural Engineering

[1]Corresponding author (e-mail: c.c.smith@sheffield.ac.uk).

 DOI: 10.1139/Zxx-xxx

able optimization across all slip-lines.

As an alternative approach, other workers (*e.g.* Fraldi & Guarracino 2009, Yang & Huang 2011, Yang & Long 2015 and Zhang & Yang 2018) used a variational approach to analyse the stability of anchors, trapdoors and tunnels with a single curved slip-line, defined by a closed form equation, that obeys the non-linear yield function flow rule along its full length. However, these analyses were restricted to single wedges constrained to move vertically and to the authors' knowledge this approach has not been extended to a wider range of problems. By extending the approach presented by Fraldi & Guarracino 2009, this paper presents a new fully general form of the variational approach for analysing translational upper bound problems using the classic multi-wedge rigid block upper bound kinematic method, based on curved slip-lines defined by closed form equations, and following the optimisation framework of *e.g.* Soon & Drescher (2007).

Examples are given for the active and passive cases of a smooth retaining wall and shown to match to within $\sim$1% of the corresponding simple non-linear lower bounds, thus for the first time giving almost exact plastic solutions for these cases. An example of how the approach can deal with a multi-wedge analysis is also given for an anchor uplift problem. An intriguing aspect of the solutions are that they give exact values of shear and normal stresses along the slip-lines, which is not normally obtained from an upper bound analysis which can only return forces on wedge interfaces. The interpretation of such values is discussed in the context of the examples studied.

2. Conventional upper bound mechanism analysis

Conventional upper bound rigid block mechanism analysis is well established in geotechnical engineering and consists of postulating a failure mechanism consisting of sliding wedges. Kinematic compatibility and an associative flow rule can be used to construct a hodograph that allows the velocities of the wedges to be determined and the relative velocities across the slip-lines computed. These can be used to determine energy dissipation on the slip-lines, and together with external work can be used to determine the collapse load. A simple two-wedge example for an anchor pullout problem (after *e.g.* Murray & Geddes 1987) is shown in Fig. 1.

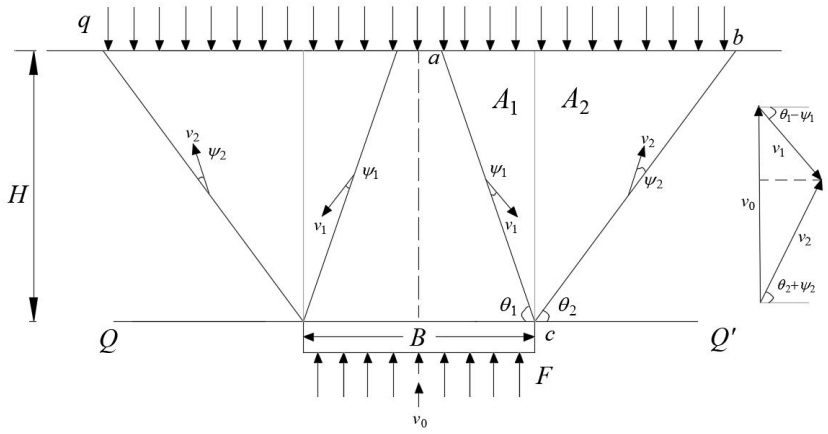

Fig. 1. Simple two-wedge anchor analysis for a linear soil showing mechanism and hodograph.

The essence of the method is to determine the angle of dilation and energy dissipation function for each slip-line. For a linear Mohr-Coulomb (c, ϕ) material of unit weight γ, the angle of dilation ψ is equal to the angle of friction ϕ for an upper bound analysis. The dissipation function for relative slip s parallel to the slip-line is cls where l is the slip-line length and $s = v\cos\psi$ where v is the relative velocity jump across the slip-line. The self weight external work for each wedge is computed

by determining the dot product of the absolute velocity of a wedge and its self weight. This together with the hodograph leads to the following equations for the two-wedge anchor analysis.

$$[1] \qquad \frac{v_0}{\sin(\theta_1+\theta_2-\psi_1+\psi_2)} = \frac{v_1}{\sin(\pi/2-\theta_2-\psi_2)} = \frac{v_2}{\sin(\pi/2-\theta_1+\psi_1)}$$

$$[2] \qquad v_{01} = v_1 \cdot \sin(\theta_1-\psi_1)$$

$$[3] \qquad v_{02} = v_2 \cdot \sin(\theta_2+\psi_2)$$

with constraints:

$$[4] \qquad \psi_1 \geq \theta_1 - \pi/2$$

$$[5] \qquad \psi_2 \leq \pi/2 - \theta_2$$

The force on the anchor can be determined from the following energy balance equation.

$$[6] \quad Fv_0 = \gamma HBv_0 + qBv_0 + 2\left(W_{A2}v_{02} + qHv_0/\tan\theta_2 - W_{A1}v_{01} + cl_{bc}v_2\cos\psi_2 + cl_{ac}v_1\cos\psi_1\right)$$

For a linear soil, the optimal solution is one for which $v_1 = 0$ and $\theta_2 = 90-\phi$, giving the following equation for F:

$$[7] \qquad \frac{F}{\gamma HB} = 1 + \frac{H}{B}\tan\phi + \frac{q}{\gamma H} + \frac{2q}{\gamma B}\tan\phi + \frac{2c}{\gamma B}$$

The aim of this paper is to demonstrate how this form of mechanism analysis for linear Mohr-Coulomb materials can be extended to a material possessing a non-linear yield surface for translational mechanisms in a fully general way.

3. Non-linear yield surface

Various non-linear strength functions have been proposed for soils and rocks, such as bilinear functions Lefebvre (1981), trilinear functions De Mello (1977) and the Hoek-Brown failure criterion Hoek & Brown (1997). Non-linear power-type failure laws for geomaterials are increasingly being adopted for investigations of the stability of geotechnical problems (*e.g.* Baker 2004, Zhang & Chen 1987, Anyaegbunam 2013).

In general, as shown in Fig. 2, a non-linear power-law failure criterion can be expressed as,

$$[8] \qquad \tau/c_0 = (a + \sigma_n/\sigma_t)^{1/m}$$

where σ_n and τ are the normal and shear stresses on the failure surface, respectively; c_0 and σ_t are normalisation stresses; and a and m are scalar constants. When $m = 1$, equation (8) reduces to the well-known linear Mohr-Coulomb failure criterion:

[9] $\tau = c + \sigma_n \tan\phi$

where $a = 1$, $c_o = c$ and $\sigma_t = c/\tan\phi$.

In this paper two exemplar non-linear materials will be modelled, representing (i) a dense sand (based on the model by Bolton 1986 using a relative density index $I_D = 1$) and (ii) a fractured rock mass (approximating a Hoek-Brown material with $\sigma_{ci} = 5$ MN/m^2, $m_i = 9.6$, $GSI = 20$, $m_b = 0.55$, Hoek & Brown 1997). The properties are given in Table 1. These were obtained by generating the relevant yield surface and carrying out a least squares best fit to equation (8). For comparison two linear soils were also modelled using (i) a simple $c = 1$ kN/m^2, $\phi = 30^o$ Mohr-Coulomb soil and (ii) a $c = 0$, $\phi = 33^o$ soil corresponding to the previous Bolton model at critical state. In both these cases, a value of $m = 1.001$ was adopted to model a closely linear system while still capable of adopting the non-linear solution methodology. It is shown in Appendix A that this leads to an error of $< 0.037\%$ in modelling the linear yield surface. Since the aim of the paper is to illustrate and verify the solution process and to contextualise it, specific engineering examples will be studied rather than undertaking parametric studies.

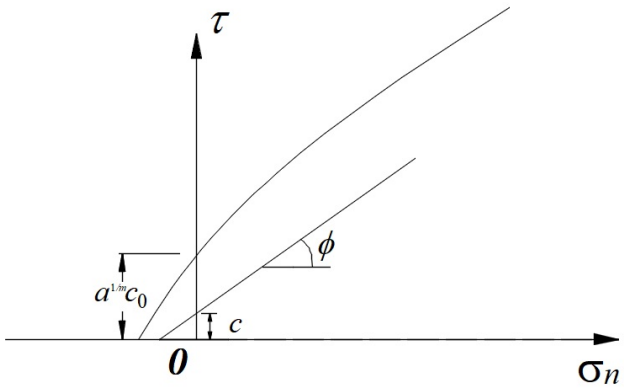

Fig. 2. Linear Mohr-Coulomb and non-linear power-law (equation 8) failure criteria.

	Linear		Non-linear	
Parameter	Cohesive-frictional soil (CF) $c = 1$ kPa, $\phi = 30^o$	Loose sand (LS) Bolton $I_D = 0$	Dense sand (DS) Bolton $I_D = 1$	Fractured rock (FR) Hoek-Brown
a(-)	1	0	0	0
c_0(kN/m^2)	1	1	1.697	1.8242×10^3
σ_t(kN/m^2)	$1/\tan 30^o$	$1/\tan 33^o$	1	5×10^3
m(-)	1.001	1.001	1.1182	1.3155
γ(kN/m^3)	15	15	15	22

Table 1. Exemplar linear and non-linear soil properties and unit weights.

4. Non-linear upper bound failure mechanism analysis for single slip-line with variational approach

Consider a slip-line, which may be curved in the general case, connecting two points A and B whose secant is orientated at an angle θ to the positive x-axis and of length l. Further consider that there is a velocity jump of v across this slip-line orientated at a fixed angle ψ_s to its secant. This velocity will therefore be orientated at an angle α to the vertical where $\alpha = \pi/2 - \kappa\psi_s - \theta$ and $\kappa = \pm 1$ denotes clockwise or anticlockwise shear respectively across the slip-line. The aim is to determine the shape of the slip-surface joining A and B which will no longer be a secant, but will curve slightly above or below the secant depending on the relative movement as shown in Fig. 3, such that the sum of the local dilation ψ and slip-line gradient at any point is constant and equal to the global slip-line dilation ψ_s. This preserves the assumption of rigid body movement of adjacent wedges. To maintain the work calculation for the general mechanism analysis similar to the linear case, a dissipation coefficient $\hat{C}$ for a non-linear material will be derived equivalent to the cohesion intercept term cl for a linear soil and where the self weight of the wedges delineated by the secants may still be used, but where the slip-line will also have its own additional self weight term $\hat{W}$ defined by the area of soil between the curved slip-line and the secant. This may be negative or positive depending on the direction of relative shear.

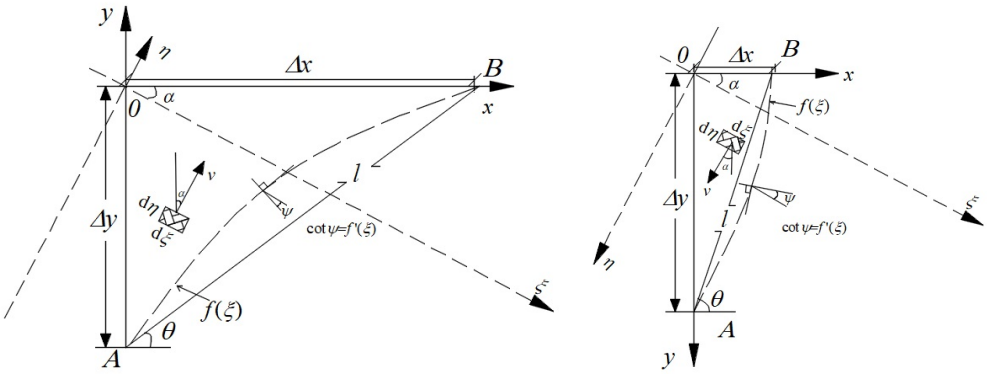

(a) Clockwise (b) Anticlockwise

Fig. 3. Non-linear kinematics of a slip-line (long-dashed line between A and B). Relative shear across slip-line: (a) clockwise; (b) anticlockwise.

4.1. General analysis form for a single slip-line

4.1.1. Compatibility

For a single slip-line as shown in Fig. 3, the mass of soil above the slip-line moves as a rigid block at velocity v and at an angle α to the vertical relative to the soil below. Let $y = f(x)$ be the equation of the velocity discontinuity surface.

This can be expressed in a rotated coordinate system as $\eta = f(\xi)$, where:

[10] $$\begin{bmatrix} \xi \\ \eta \end{bmatrix} = \begin{bmatrix} \cos\alpha & -\sin\alpha \\ \sin\alpha & \cos\alpha \end{bmatrix} \begin{bmatrix} x \\ y \end{bmatrix}$$

Use of this new coordinate system simplifies the subsequent analysis by making the velocity v parallel to the η axis. By assuming the plastic potential, ς, to be coincident with the Mohr envelope and considering τ is positive, the following can be defined:

$$[11] \quad \varsigma = \tau - c_0(a + \sigma_n/\sigma_t)^{1/m}$$

Adapting the approach developed for a tunnel analysis in a Hoek-Brown material by Fraldi & Guarracino (2009), and assuming associative flow, the local angle of dilation ψ may be given by the following equation:

$$[12] \quad \tan\psi = \frac{d\tau}{d\sigma_n} = \frac{c_0(a + \sigma_n/\sigma_t)^{\frac{1-m}{m}}}{m\sigma_t}$$

and because relative movement of the block above the discontinuity is parallel to the η-axis, the following can also be written:

$$[13] \quad \tan\psi = \frac{1}{\kappa f'(\xi)}, \quad \cos\psi = \kappa f'(\xi)\left[1 + f'(\xi)^2\right]^{-\frac{1}{2}}, \quad \sin\psi = \left[1 + f'(\xi)^2\right]^{-\frac{1}{2}}$$

where $\kappa = 1$ for the clockwise relative shear case and $\kappa = -1$ for the anti-clockwise relative shear case.

Combining equations (12) and (13) gives

$$[14] \quad \sigma_n = -a \cdot \sigma_t + \sigma_t \left(\frac{c_0}{m\sigma_t}\right)^{\frac{m}{(m-1)}} \left[\kappa f'(\xi)\right]^{\frac{m}{(m-1)}}$$

and substitution in equation (8) gives,

$$[15] \quad \tau = c_0 \left(\frac{c_0}{m\sigma_t}\right)^{\frac{1}{(m-1)}} \left[\kappa f'(\xi)\right]^{\frac{1}{(m-1)}}$$

Now the plastic strain rates can be written as follows:

$$[16] \quad \dot{\varepsilon}_n = \lambda\frac{\partial\varsigma}{\partial\sigma} = -\lambda\frac{c_0}{m\sigma_t}(a + \sigma_n/\sigma_t)^{(1-m)/m}$$

$$[17] \quad \dot{\gamma} = \lambda\frac{\partial\varsigma}{\partial\tau} = \lambda$$

where λ is a scalar parameter, $\dot{\varepsilon}_n$ is the normal plastic strain rate and $\dot{\gamma}$ is the shear plastic strain rate. Based on the kinematics occurring on the slip-line, as shown in Fig. 3, the plastic strain rate components can also be written in the form

$$[18] \quad \dot{\varepsilon}_n = v_n = -\frac{v}{w}\left[1 + f'(\xi)^2\right]^{-\frac{1}{2}}$$

$$[19] \quad \dot{\gamma} = v_t = \frac{v}{w}\kappa f'(\xi)\left[1 + f'(\xi)^2\right]^{-\frac{1}{2}}$$

where $\eta = f(\xi)$ is the function of velocity discontinuity surface and $f'(\xi)$ is the first derivative of $f(\xi)$. v is the velocity jump at the slip-line and w is the thickness of the plastic zone (assumed infinitesimal).

A dot denotes differentiation with respect to time and a prime with respect to ξ, i.e. $v = \partial u/\partial t$, $f'(\xi) = \partial f(\xi)/\partial \xi$

In order to enforce compatibility, from equation (17) and equation (19) (or, equivalently from equation (14), equation (16) and equation (18)) it follows that:

$$\lambda = \frac{v}{w}\kappa f'(\xi)\left[1 + f'(\xi)^2\right]^{-\frac{1}{2}} \tag{20}$$

4.1.2. Determination of internal energy dissipation and external work

Based on the plastic potential function equation (11), the plastic strain increment is proportional to the gradient of the plastic potential function through the associated flow rule. The dissipation energy associated with the internal forces at any point on the surface, $\dot{D}_i$ can therefore be obtained by combining equation (14), equation (15), equation (18) and equation (19):

$$\dot{D}_i = \sigma_n v_n + \tau v_t = \frac{v}{w}\left[1 + f'(\xi)^2\right]^{-\frac{1}{2}}\left[a \cdot \sigma_t + \sigma_t\left(\frac{c_0}{m\sigma_t}\right)^{\frac{m}{(m-1)}}(m-1)[\kappa f'(\xi)]^{\frac{m}{(m-1)}}\right] \tag{21}$$

By considering the profile of failure surface for the single wedge, as shown in Fig. 3 the energy dissipation along the velocity discontinuity surface can be obtained by integrating $\dot{D}_i$ over the interval $\xi = \Delta y \sin\alpha$ to $\Delta x \cos\alpha$ where $\Delta x = l\cos\theta$ and $\Delta y = l\sin\theta$.

Hence

$$\begin{aligned} D &= \int_{\Delta y \sin\alpha}^{\Delta x \cos\alpha} \dot{D}_i w \sqrt{1 + f'(\xi)^2}\, d\xi \\ &= v\int_{\Delta y \sin\alpha}^{\Delta x \cos\alpha}\left\{a \cdot \sigma_t + \sigma_t\left(\frac{c_0}{m\sigma_t}\right)^{\frac{m}{(m-1)}}(m-1)[\kappa f'(\xi)]^{\frac{m}{(m-1)}}\right\} d\xi \end{aligned} \tag{22}$$

The work done (W_e) by the external force (gravity) on the area between the curve and the secant is given as follows (NB in the active case, the area is negative, but the integration is also negative.):

$$W_e = \kappa v\gamma\cos\alpha\left[\int_{\Delta y \sin\alpha}^{\Delta x \cos\alpha} f(\xi)d\xi + \Delta y\cos\alpha(\Delta x\cos\alpha - \Delta y\sin\alpha) - 0.5l^2\sin(\theta+\alpha)\cos(\theta+\alpha)\right] \tag{23}$$

4.1.3. Solution characterizing optimal slip-line geometry

In order to describe the optimal shape of the slip-line, it is necessary to obtain the explicit expression of $f(\xi)$ by constructing an objective function Λ consisting of the sum of the contribution of the slip-line to the external work rate and the rate of the internal energy dissipation,

$$\begin{aligned} \Lambda &= D - W_e \\ &= v\int_{\Delta y \sin\alpha}^{\Delta x \cos\alpha} \zeta[f(\xi), f'(\xi), \xi]d\xi \\ &\quad - v\kappa\gamma\cos\alpha\left[\Delta y\cos\alpha(\Delta x\cos\alpha - \Delta y\sin\alpha) - 0.5l^2\sin(\theta+\alpha)\cos(\theta+\alpha)\right] \end{aligned} \tag{24}$$

in which

$$[25] \quad \zeta[f(\xi), f'(\xi), \xi] = \sigma_t \left[a + \left(\frac{c_0}{m\sigma_t} \right)^{\frac{m}{(m-1)}} (m-1)[\kappa f'(\xi)]^{\frac{m}{(m-1)}} \right] - \kappa\gamma f(\xi)\cos\alpha$$

In order to obtain the effective failure surface for a given slip-line of angle θ and length l, it is necessary to search for the extremum value of objective function Λ using Euler's equation through the variational method. The expression of the variational equation of Λ for stationary conditions can be written as:

$$[26] \quad \frac{\partial \Lambda}{\partial f(\xi)} - \frac{\partial}{\partial \xi}\left[\frac{\partial \Lambda}{\partial f'(\xi)} \right] = 0$$

and the explicit form of the Euler's equation for the equation (25) can thus be obtained as:

$$[27] \quad \kappa\gamma\cos\alpha + \frac{m\sigma_t}{(m-1)} \left(\frac{c_0}{m\sigma_t} \right)^{\frac{m}{m-1}} [\kappa f'(\xi)]^{\frac{2-m}{m-1}} [f''(\xi)] = 0$$

Equation (27) is a non-linear second-order homogeneous differential equation. A first integration yields

$$[28] \quad m\sigma_t \left(\frac{c_0}{m\sigma_t} \right)^{\frac{m}{m-1}} [\kappa f'(\xi)]^{\frac{1}{m-1}} = -\kappa\gamma\cos\alpha \cdot \xi + n_0$$

where n_0 is integration constant coefficient. Re-arrangement of this equation gives:

$$[29] \quad f'(\xi) = \kappa m k_0 (\frac{n_0}{\gamma \cdot \cos\alpha} - \kappa\xi)^{m-1}$$

in which

$$[30] \quad k_0 = \frac{\sigma_t}{\gamma\cos\alpha} \left(\frac{\gamma \cdot \cos\alpha}{c_0} \right)^m = \frac{\sigma_t}{c_0} \left(\frac{\gamma \cdot \cos\alpha}{c_0} \right)^{m-1} = \frac{\sigma_t}{c_0^m} (\gamma\cos\alpha)^{m-1}$$

By a further integral calculation process the equation for the velocity discontinuity surface is given by:

$$[31] \quad f(\xi) = -k_0 (\frac{n_0}{\gamma \cdot \cos\alpha} - \kappa\xi)^m + n_1$$

and a further integration provides an expression required later for the weight correction term:

$$[32] \quad \int f(\xi).d\xi = \frac{\kappa k_0}{m+1} (\frac{n_0}{\gamma \cdot \cos\alpha} - \kappa\xi)^{m+1} + n_1\xi + \text{const}$$

where n_0 and n_1 are two unknowns representing the integration constant coefficients. These can be determined using the two boundary conditions:

[33] $$f(\xi = \Delta y \sin\alpha) = -\Delta y \cos\alpha$$

[34] $$f(\xi = \Delta x \cos\alpha) = \Delta x \sin\alpha$$

Hence:

[35] $$-k_0(\frac{n_0}{\gamma\cos\alpha} - \kappa\Delta x\cos\alpha)^m + n_1 - \Delta x\sin\alpha = 0$$

and

[36] $$n_1 = -\Delta y \cdot \cos\alpha + k_0(\frac{n_0}{\gamma\cdot\cos\alpha} - \kappa\Delta y\cdot\sin\alpha)^m$$

It is not possible to derive closed form expressions for n_0 and n_1, however by substituting equation (36) into equation (35), these may be determined straightforwardly numerically using standard root finding algorithms. There is a small range of values of α and hence ψ_s that will give valid solutions.

This solution may be expressed as a dilation (relative to the secant) of $\psi_s = \kappa(\pi/2 - \alpha - \theta)$, a coefficient of dissipation $\hat{C}(\psi_s, \theta, l)$ based on equation (22) and a correction to the wedge weight above the slip-line $\hat{W}(\psi_s, \theta, l)$ based on equation (23). $\hat{C}$ is equivalent to the term cl for the linear case. Thus $\hat{C}$ is multiplied by $s = v\cos\psi_s$ to give the full dissipation. Hence expressions for $\hat{C}$ and $\hat{W}$ can be written in terms of the derived function f:

From equation (22):

[37]
$$\hat{C}(\psi_s,\theta,l) = \frac{\kappa\sigma_t}{\cos\psi_s}\left(\frac{m-1}{m+1}\right)\left(\frac{\gamma\cos\alpha}{c_0}\right)^m[(\frac{n_0}{\gamma\cos\alpha} - \kappa\Delta y\sin\alpha)^{m+1} - (\frac{n_0}{\gamma\cos\alpha} - \kappa\Delta x\cos\alpha)^{m+1}] + a\cdot\frac{\sigma_t}{\cos\psi_s}(\Delta x\cos\alpha - \Delta y\sin\alpha)$$

and from equation (23) and equation (32):

[38]
$$\frac{\hat{W}(\psi_s,\theta,l)}{\kappa\gamma} = \frac{\kappa k_0}{m+1}[(\frac{n_0}{\gamma\cos\alpha} - \kappa\Delta x\cos\alpha)^{m+1} - (\frac{n_0}{\gamma\cos\alpha} - \kappa\Delta y\sin\alpha)^{m+1}] + n_1(\Delta x\cos\alpha - \Delta y\sin\alpha) + \Delta y\cos\alpha(\Delta x\cos\alpha - \Delta y\sin\alpha) - 0.5l^2\sin(\theta+\alpha)\cos(\theta+\alpha)$$

These functions are straightforward to compute using a spreadsheet or computer program.

5. General solution procedure

The following outlines a typical hand solution process following the standard form of linear upper bound wedge analysis.

1. Postulate an appropriate multi-wedge failure mechanism, involving a series of nodes linking slip-lines that delineate each wedge, allocating an appropriate value of global dilation ψ_s to each slip-line. ψ_s must be chosen to generate real values of n_0 and n_1 for each slip-line.

2. Based on the straight lines joining each node and the values of ψ_s, draw the corresponding hodograph.

3. Determine the acting weight W of each wedge based on the area of the wedge delineated by straight lines joining each node, and adjusted according to the term $\hat{W}$ for each slip-line edge of the wedge.

4. Determine the external work done using the velocities from the hodograph and the weight of each wedge, and the external live and dead loads.

5. Determine the internal energy dissipation $\hat{C}v\cos\psi_s$ based on the relative velocities v across each slip-line.

6. Equate external work and internal energy dissipation to determine the live load.

6. Application to specific problems

Having derived a generic solution process, its application will be illustrated through a range of specific geotechnical problem types: (i) active/passive smooth retaining wall, and (ii) an anchor/trapdoor. This may be done by deriving the full energy equation for the specific problem and then minimising the energy by varying the assumed values of wedge angle and dilation angle ψ_s for each slip-line, to give the optimal upper bound for the slip-line mechanism. In this note, the optimization of the upper bound solution is carried out numerically using MATLAB's built in multi-parameter minimisation functions.

6.1. Active and passive retaining wall

Consider a frictionless vertical wall of height H with horizontal active or passive load F, and a surface surcharge q with a single wedge at angle θ to the horizontal and of area $0.5H^2/\tan\theta$ as shown in Fig. 4 together with the hodograph. The slip-line length $l = H/\sin\theta$.

If the dilation is assumed to be ψ_s, the wedge moves at a velocity v_0 at an angle $\theta + \kappa\psi_s$ to the horizontal and the full energy equation may be expressed as:

$$[39]\quad F\kappa v_0\cos(\theta+\kappa\psi_s) = \left[\frac{H^2\gamma}{2\tan\theta} - \kappa\hat{W}(\psi_s,\theta,l) + \frac{qH}{\tan\theta}\right]\kappa v_0\sin(\theta+\kappa\psi_s)+\hat{C}(\psi_s,\theta,l)v_0\cos\psi_s$$

This is identical to a conventional linear analysis with the addition of the $\hat{W}$ term and the replacement of the cl term by $\hat{C}$. To find the optimal upper bound, it is necessary to find max $F(\psi_s,\theta)$ for the active case and min $F(\psi_s,\theta)$ for the passive case.

The optimization must thus be done in two parameters rather than the one (θ) for the linear problem and is straightforward to carry out numerically using equation (39). Solutions using the example parameter sets given in Table 1, are given in Table 2. A single maximum/minimum exists in each case as shown in Fig. 5 for the fractured rock material. Note that the solutions assume that tensile stresses are sustainable on the back of the wall for the cohesive-frictional soil.

Each model was checked against a simple Rankine lower bound based on the non-linear yield surface (see Appendix B). Very close matches were found for the approximately linear materials as expected, and matches within $\sim$1% for the non-linear materials. The values thus bracket the true solution very closely. Comparison of the lower bound solutions to the known linear solution for the first two materials show they are close. Further checks show that they do converge as would be expected as m is reduced towards 1.0.

Fig. 6 shows the feasible range of optimal slip-lines for the passive wall fractured rock case for different values of θ with the optimum value of ψ_s in each case annotated on each line.

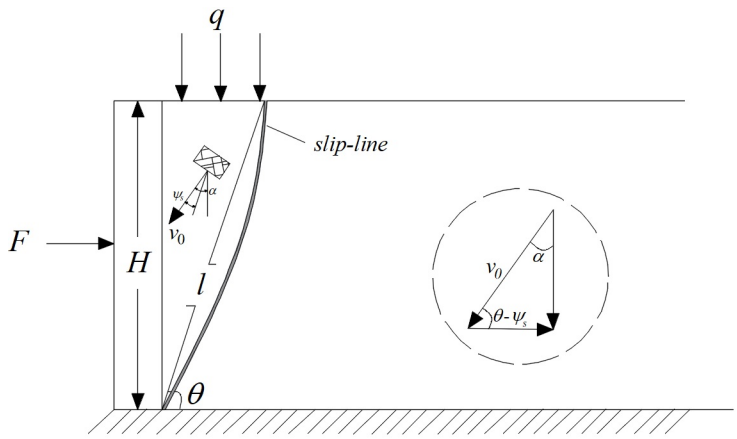

(a) Active

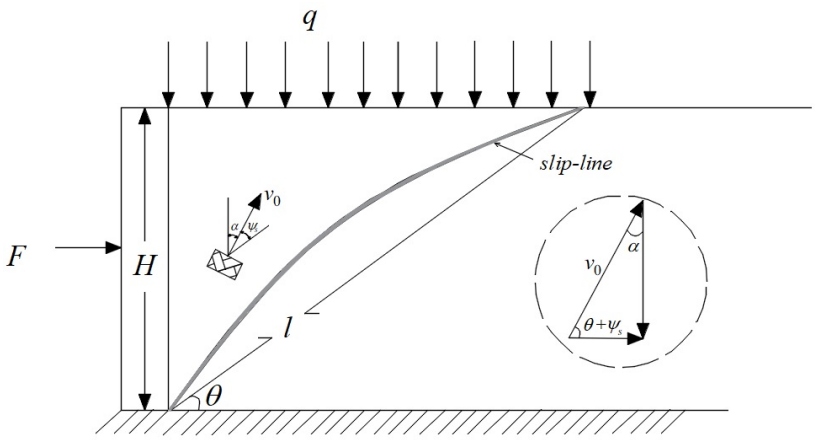

(b) Passive

Fig. 4. Failure mechanism analysis for smooth retaining wall with surcharge load.

Failure mode	Parameter set	θ_{opt}	$\psi_{s,opt}$	n_0	F_{upper} (kN/m)	F_{lower} (kN/m)	% difference	F_{linear} (kN/m)
Active	CF	59.96^o	29.92^o	-8.927	65.2573	65.2573	0.000	65.05983
	LS	61.46^o	32.91^o	-7.836	62.8278	62.8278	0.000	62.6451
	DS	70.90^o	50.78^o	-1.5629	23.8231	23.8633	0.169	-
	FR	71.99^o	51.24^o	-2.791	26.8704	27.3218	1.680	-
Passive	CF	30.05^o	29.89^o	102.93	652.3262	652.3262	0.000	654.8205
	LS	28.56^o	32.88^o	111.32	717.7809	717.7809	0.000	720.8255
	DS	22.38^o	44.39^o	168.81	1349.0075	1347.7533	0.093	-
	FR	26.18^o	36.10^o	201.42	1511.5016	1506.3272	0.342	-

Table 2. Retaining wall solutions for the case $q = 5$ kN/m^2, and $H = 5$m, using material properties from Table 1. The values of F_{linear} are computed using conventional Rankine equations for a smooth retaining wall where *e.g.* $\sigma'_h = K_a\sigma'_v - K_{ac}c'$, $K_a = \tan^2(\pi/4 - \phi/2)$ and $K_{ac} = 2\sqrt{K_a}$, and similarly for the passive case.

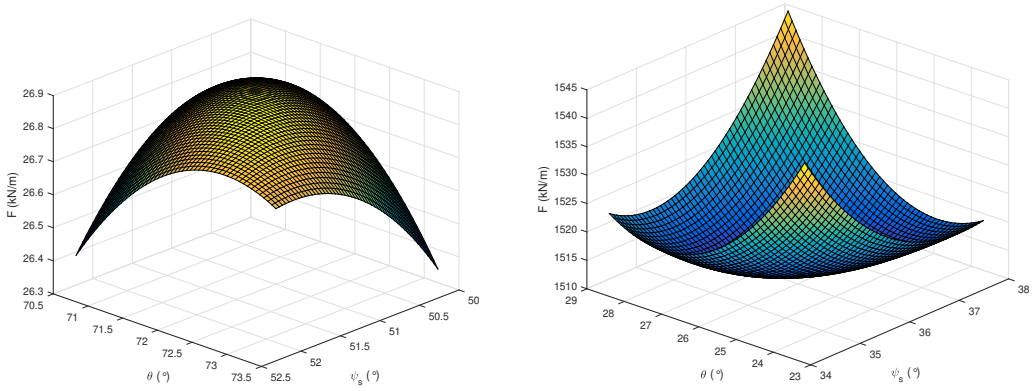

(a) Active (b) Passive

Fig. 5. Variation of thrust F with θ and ψ_s for a smooth retaining wall with surcharge load for the fractured rock material (properties given in Table 1) and $q = 5$ kN/m^2, and $H = 5$m.

To put the results into context in comparison with a conventional linear analysis, a simple conservative analysis of the fractured rock problem could be carried out using a secant angle of friction across a suitable stress range. The non-linear lower bound analysis in Appendix B predicts a horizontal stress of ~ 450 kN/m^2 at the wall base for the fractured rock parameters. Thus, selecting a range of 0 to 450 kN/m^2, which roughly spans the range of stresses expected in the problem, gives a secant angle of 33^o (almost the same as the loose sand material). This gives a passive load of 1017 kN/m using a simple Rankine analysis (using the fractured rock self weight of 22 kN/m^3, and the linear angle of shearing resistance of 33^o). This is about 2/3 of the non-linear result.

6.2. Anchor/trapdoor (two-wedge)

The general approach is now illustrated with a two-wedge analysis for an anchor/trapdoor following the geometry shown in Fig. 1 and adopting an anchor width $B = 5$m.

There are now four variables to be optimised which are θ_1, θ_2, ψ_{s1} and ψ_{s2} . The hodograph and corresponding equations (1) - (5) remain the same as for the linear case and equation (6) is extended to

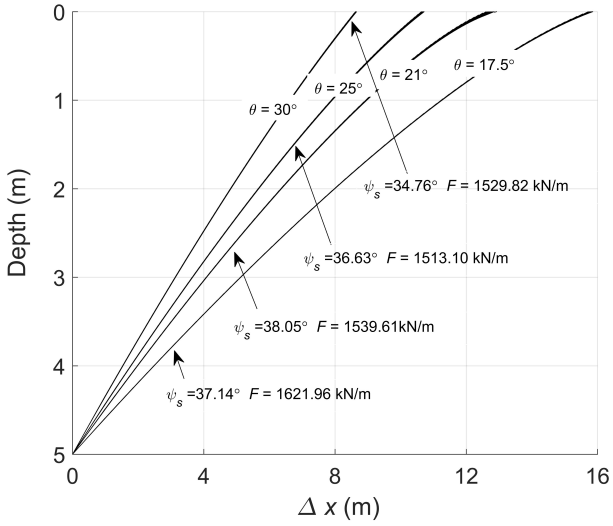

Fig. 6. Sample set of possible passive slip-lines for fractured rock case for different values of θ and with ψ_s optimized for this value of θ (the actual feasible range of values for θ ranges between 0.1^o and 84^o).

the following:

$$
\begin{aligned}
Fv_0 =& \gamma HBv_0 + qBv_0 + 2qHv_0/\tan\theta_2 + 2[W_{B2}\cdot v_{02} - \hat{W}(\psi_{s2},\theta_2,l_2)\cdot v_2 - W_{B1}\cdot v_{01} \\
& - \hat{W}(\psi_{s1},\theta_1,l_1)\cdot v_1 + \hat{C}(\psi_{s2},\theta_2,l_2)v_2\cos\psi_{s2} + \hat{C}(\psi_{s1},\theta_1,l_1)v_1\cos\psi_{s1}]
\end{aligned}
\tag{40}
$$

where $l_1 = H/\sin\theta_1$ and $l_2 = H/\sin\theta_2$.

Parameter set	θ_1	ψ_{s1}	θ_2	ψ_{s2}	F_{upper}(kN/m)	F_{prev} (kN/m)
Cohesive frictional	any	any	60.00^o	29.99^o	655.28	655.29
Loose sand	any	any	57.00^o	32.99^o	675.05	675.05
Dense sand	any	any	43.78^o	46.22^o	878.51	879.45
Fractured rock	any	any	49.45^o	40.55^o	1188.40	1190.00

Table 3. Two-wedge anchor solutions for the case $q = 5$ kN/m^2, and $H = 5$m, using material properties from Table 1. F_{prev} are values computed using the approach of Fraldi & Guarracino (2009), for the non-linear soils and using equation (6) for the linear soils.

To illustrate the general behaviour, first a solution where all four parameters θ_1, θ_2, ψ_{s1} and ψ_{s2} are fixed is shown in Fig. 7. Solutions were then investigated where the solution was optimised for all four parameters. However, it was found that the optimal solution was always that for which $\theta_2+\psi_{s2} = \pi/2$, independent of the values of θ_1 and ψ_{s1} as shown in Table 3 for each of the soil types in Table 1. From the hodograph in Fig. 1, v_1 must be zero if $\theta_2 + \psi_{s2} = \pi/2$ and $\theta_1 - \psi_{s1}$ can take on any value. This agrees well with the linear case (*e.g.* Murray & Geddes 1987). There are no known non-linear lower bound solutions to the anchor problem. A linear lower bound solution was derived by Smith (1998) and gives an almost identical answer as the upper bound result in equation (6).

An illustration of the variation of the results for fixed $\theta_1 = 63.43^o$ and $\psi_{s1} = 20.0^o$ with θ_2 and ψ_{s2} allowed to vary, are shown graphically in Fig. 8 for the fractured rock case and shows there is one minimum solution. In Fig. 8 the magenta dot represents the solution for $\theta_2 = 50^o$ and $\psi_{s2} = 25^o$ for fixed $\theta_1 = 63.43^o$ and $\psi_{s1} = 20.0^o$ corresponding to the mechanism in Fig. 7.

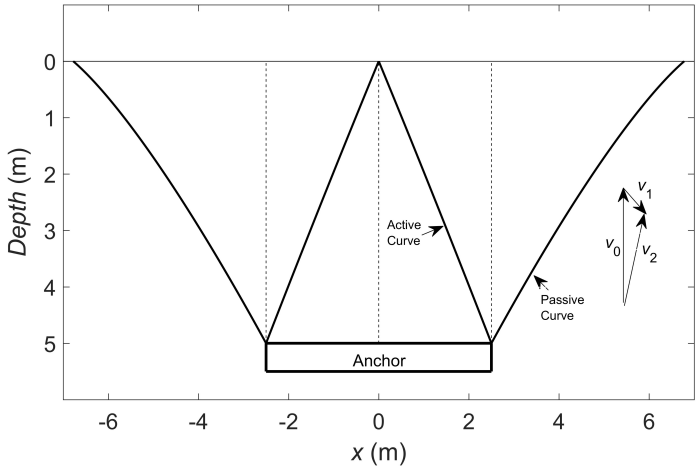

Fig. 7. Example results of non-linear analysis showing mechanism and hodograph for two-wedge anchor embedded in fractured rock (properties given in Table 1) with $q = 5$ kN/m^2 and $H = 5$m. The active curves were selected to meet at the surface on the symmetry line and use a specified dilation angle: $\theta_1 = 63.43^o$, $\psi_{s1} = 20^o$. The passive curve used values $\theta_2 = 50^o$ and $\psi_{s2} = 25^o$. The predicted upper bound load $F = 2323.0$ kN/m^2.

7. Discussion

The above examples clearly illustrate how the method may be applied to a general multiple-wedge rigid-block analysis, giving it a very broad applicability, and has verified it against lower bound and other solutions in the literature. Essentially the method replicates the nature of a conventional linear soil analysis, but doubles the number of variables to be optimised (slip-line orientation and equivalent dilation on the slip-line), in cases where optimization is required. The examples shown which were of a smooth retaining wall and anchor uplift display similar characteristics as for their linear counterparts.The optimal smooth retaining wall single line upper bound solution is very close to the true solution, and the optimal two-wedge anchor solution reduces to a single wedge solution.

The approach presented in this paper determined the optimal upper bound by full application of the conventional energy minimisation approach. This is in contrast to some previous authors *e.g.* Fraldi & Guarracino (2009, 2010, 2011), Yang & Huang (2011), Zhang & Yang (2018)) who adopted a partial optimization of energy minimisation to obtain a variational form of the slip-line but then used a stress boundary condition at the soil surface to complete the solution. This assumed that the slip-line had to meet the (horizontal) surface at an angle consistent with a simple active or passive Rankine stress state at the surface. Solutions invoking such a boundary condition are still valid upper bounds, but were found to give collapse loads approx 0.3% higher than the full minimization approach as used in this paper as shown in Table 3. While this boundary condition assumption may be valid for the smooth retaining wall problem, it does not hold universally. In reality it is expected that the anchor/trapdoor

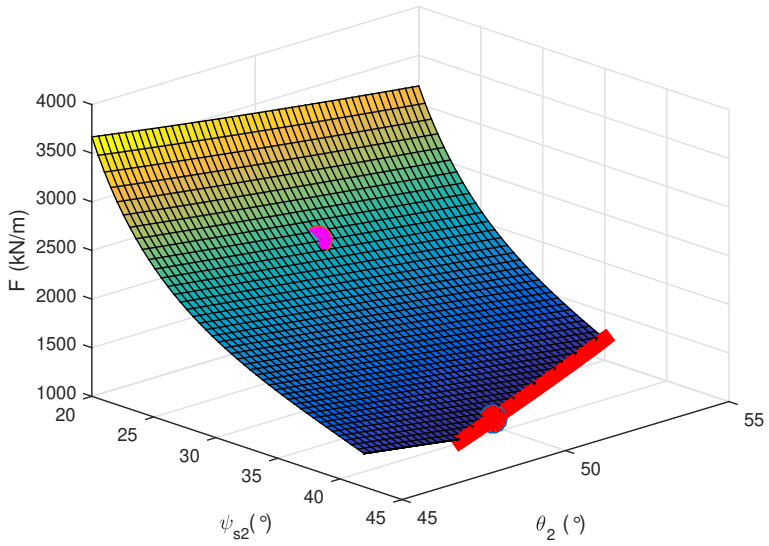

Fig. 8. Variation of limit load F with fixed values of $\theta_1 = 63.43^o$ and $\psi_{s1} = 20.0^o$ for the fractured rock case (properties given in Table 1) and $q = 5$ kN/m^2, $H = 5$m and $B = 5$m. The red line represents the kinematic limits of feasibility for the problem (equation 5). The optimal solution (red dot) lies on this line. At lower values of θ_2, the solution is limited by feasibility of the non-linear solution. The magenta dot represents the solution depicted in Fig. 7 for $\theta_2 = 50^o$ and $\psi_{s2} = 25^o$.

.

stress field would involve a singularity at the point where the slip-line meets the surface with rotations of the principle stress directions around this point as demonstrated by Smith (1998) for the linear soil case.

The solution also assumed that the shape of the non-linear slip-line could be described by a function $y = f(x)$. This assumption gives a relatively simple solution. There may be scope to achieve higher degrees of freedom in the solutions by adopting a parametric curve $f_p(x, y) = 0$, however this is beyond the scope of the present work.

One intriguing aspect of the analysis as pointed out by Baker & Frydman (1983) and Chen (1975) is that the upper bound solution not only identifies the slip-line geometry, but also part of the stress state at every point along the line, using equation (14) and equation (8), since each point has a unique gradient. It is thus possible to plot the shear stress and/or normal stress on the line with depth as shown in Fig. 9 and Fig. 10. For the active and passive walls, these values match reasonably closely to the values predicted by the lower bound approach (as would be expected). Note that the plotted lower bound values are those corresponding to the yield condition predicted by the lower bound at the relevant depth.

For the anchor, the normal stress follows a value $\sigma_n =\sim 1.0\gamma z$. This is consistent with the order of magnitude of values found in the stress rotation model of Smith (1998) for an anchor in a linear soil. While the optimal mechanism is expected to involve multiple slip-lines, the single slip-line solution is expected to be close to optimal, in a similar way to the linear soil case, and the corresponding stress state is expected to be close to the true solution result, but not exact. This example clearly shows that the predicted stresses are of the order expected and may be valuable in identifying the nature of lower bound solutions, or stresses acting on structures. Further work, however, is required in this area.

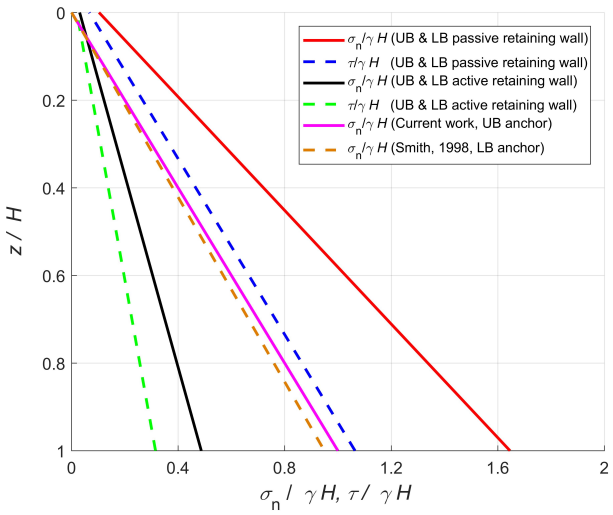

Fig. 9. Predicted upper bound (UB) and lower bound (LB) normalised normal and shear stresses for anchor ($q = 0$kN/m^2 and $H = 5$m) and active and passive retaining wall cases ($q = 5$kN/m^2 and $H = 5$m): loose sand case. Wall UB and LB solutions are coincident.

Finally while the work here has been presented in the context of a classical hand calculation with simple optimization of a few variables, it should be possible to incorporate the approach into the much more general computational rigid block analysis approach Discontinuity Layout Optimization (Smith & Gilbert 2007) to produce solutions of high accuracy and to also extend the approach to cover rotational mechanisms in addition to translational mechanisms.

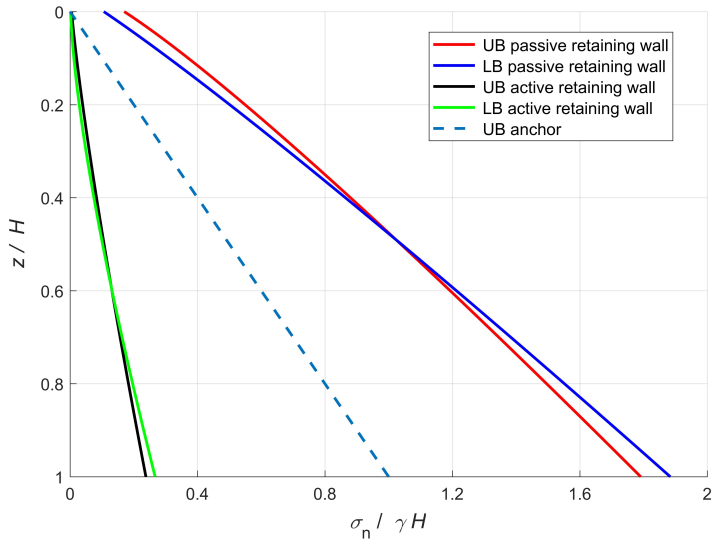

Fig. 10. Predicted upper bound (UB) and lower bound (LB) normalised normal stresses for anchor ($q = 0$kN/m^2 and $H = 5$m) and active and passive retaining wall cases ($q = 5$kN/m^2 and $H = 5$m): fractured rock case (NB no lower bound anchor solution is available for this case).

8. Conclusions

1. A fully general variational approach for the upper bound analysis of geotechnical collapse mechanisms in non-linear soils has been presented. The analysis follows the form of the classic upper bound multi-wedge analysis utilised for linear soils. It is based on the use of closed form equations and only requires the numerical solution of a single implicit equation in one variable.

2. The approach presented has significantly extended a methodology developed previously for the special case of deep tunnels and the anchor/trapdoor problem, and used full energy optimisation of the solution, rather than adopting a special boundary condition.

3. Application of the method to the analysis of active and passive earth pressures acting on a smooth retaining wall, demonstrated that the single wedge solutions obtained gave results very close to a simple lower bound analysis and thus established a close bracket to the true plastic solution for this case.

4. A further example addressing the anchor uplift problem demonstrated the solution process for multi-wedges and showed that the solution behaviour follows a similar pattern to that for linear soils. More accurate solutions for this problem were obtained compared to previous work in the literature.

5. Due to the non-linearity of the yield surface, for the simple types of solution utilised here, it is possible to determine the normal and shear stresses at any point on the slip-line. This is not normally available for upper bound problems. The validity of these stresses has been investigated and show strong consistency with related lower bound solutions, but further work is required in this area to establish the validity of the values generated.

References

Anyaegbunam, A. J. (2013), 'Nonlinear power-type failure laws for geomaterials: Synthesis from triaxial data, properties, and applications', *International Journal of Geomechanics* **15**(1), 04014036.

Baker, R. (2004), 'Nonlinear mohr envelopes based on triaxial data', *Journal of Geotechnical and Geoenvironmental Engineering* **130**(5), 498–506.

Baker, R. & Frydman, S. (1983), 'Upper bound limit analysis of soil with non-limear failure criterion', *Soils and Foundations* **23**(4), 34–42.

Bolton, M. (1986), 'The strength and dilatancy of sands', *Geotechnique* **36**(1), 65–78.

Chen, W.-F. (1975), *Limit Analysis and Soil Plasticity*, Vol. 7 of *Developments in Geotechnical Engineering*, Elsevier Scientific Publishing Company.

Chen, W. & Liu, X. (1990), *Limit Analysis in Soil Mechanics*, Vol. 41 of *Developments in Geotechnical Engineering*, Elsevier.

De Mello, V. F. (1977), 'Reflections on design decisions of practical significance to embankment dams'.

Fraldi, M. & Guarracino, F. (2009), 'Limit analysis of collapse mechanisms in cavities and tunnels according to the hoek–brown failure criterion', *International Journal of Rock Mechanics and Mining Sciences* **46**(4), 665–673.

Fraldi, M. & Guarracino, F. (2010), 'Analytical solutions for collapse mechanisms in tunnels with arbitrary cross sections', *International Journal of Solids and Structures* **47**(2), 216–223.

Fraldi, M. & Guarracino, F. (2011), 'Evaluation of impending collapse in circular tunnels by analytical and numerical approaches', *Tunnelling and Underground Space Technology* **26**(4), 507–516.

Hambleton, J. & Sloan, S. (2013), 'A perturbation method for optimization of rigid block mechanisms in the kinematic method of limit analysis', *Computers and Geotechnics* **48**, 260–271.

Hoek, E. & Brown, E. T. (1997), 'Practical estimates of rock mass strength', *International Journal of Rock Mechanics and Mining Sciences* **34**(8), 1165–1186.

Lefebvre, G. (1981), 'Fourth canadian geotechnical colloquium: Strength and slope stability in canadian soft clay deposits', *Canadian Geotechnical Journal* **18**(3), 420–442.

Mohammadi, M. & Tavakoli, H. (2015), 'Comparing the generalized hoek-brown and mohr-coulomb failure criteria for stress analysis on the rocks failure plane', *Geomechanics and Engineering* **9**(1), 115–124.

Murray, E. & Geddes, J. D. (1987), 'Uplift of anchor plates in sand', *Journal of Geotechnical Engineering* **113**(3), 202–215.

Smith, C. C. (1998), 'Limit loads for an anchor/trapdoor embedded in an associative coulomb soil', *International Journal for Numerical and Analytical Methods in Geomechanics* **22**(11), 855–865.

Smith, C. & Gilbert, M. (2007), 'Application of discontinuity layout optimization to plane plasticity problems', *Proceedings of the Royal Society of London A: Mathematical, Physical and Engineering Sciences* **463**(2086), 2461–2484.

Soon, S.-C. & Drescher, A. (2007), 'Nonlinear failure criterion and passive thrust on retaining walls', *International Journal of Geomechanics* **7**(4), 318–322.

Ukritchon, B. & Keawsawasvong, S. (2018), 'Three-dimensional lower bound finite element limit analysis of hoek-brown material using semidefinite programming', *Computers and Geotechnics* **104**, 248 – 270.

Yang, X. & Huang, F. (2011), 'Collapse mechanism of shallow tunnel based on nonlinear hoek–brown failure criterion', *Tunnelling and Underground Space Technology* **26**(6), 686–691.

Yang, X. & Long, Z. (2015), 'Roof collapse of shallow tunnels with limit analysis method', *Journal of Central South University* **22**, 1929–1936.

Zhang, R. & Yang, X. (2018), 'Limit analysis of active and passive mechanisms of shallow tunnels in nonassociative soil with changing water table', *International Journal of Geomechanics* **18**(7), 04018063.

Zhang, X. & Chen, W. (1987), 'Stability analysis of slopes with general nonlinear failure criterion', *International Journal for Numerical and Analytical Methods in Geomechanics* **11**(1), 33–50.

Appendix A: Non-linear approximation of a linear yield function

For validation purposes and also in order to access the stress values along a slip-line, it is useful to use the non-linear model described to represent a linear system by adopting a value of m very close to 1.0. The accuracy of this approximation can be calculated as follows:

Taking $a = 0$ for simplicity, the following can be written

$$\tau = c_0(\sigma_n/\sigma_t)^{1/m} \quad [41]$$

Let this equation and the linear form $\tau = c_{0l}(\sigma_n/\sigma_t)$ intersect at the origin and when $\sigma_n = \sigma_{n1}$. This defines the range of the approximation. Thus

$$c_{0l} = c_0(\sigma_{n1}/\sigma_t)^{(1-m)/m} \quad [42]$$

The difference between the linear and non-linear curves at any value of σ_n, as a proportion of the intersection value at σ_{n1} is given by:

$$\frac{c_0(\sigma_n/\sigma_t)^{1/m} - c_{0l}(\sigma_n/\sigma_t)}{c_0(\sigma_{n1}/\sigma_t)^{1/m}} \quad [43]$$

A plot of this function shows that this has a maximum at around $0.4\bar{\sigma}$ and is approximately equal to $0.37 \times (m-1)$ for small $m-1$.

Appendix B: Lower bound solution for a smooth retaining wall

For a smooth wall with vertical soil/wall interface, the same simple stress state configuration may be used for a non-linear soil as for a linear soil, namely the assumption that principal stresses are horizontal and vertical. The vertical stresses may thus be predicted by the following simple equation:

$$\sigma_v = q + \gamma z \quad [44]$$

where q is the surface surcharge and z is the depth below the surface. Hence drawing the largest or smallest Mohr's circle through this point that touches the non-linear yield surface will determine the passive and active lateral earth pressures respectively. Depending on the nature of the yield surface, the circle may be limited by a tangent to the main curve, or by the apex of the yield surface when $\tau = 0$. Given that:

$$\tau = c_0(a + \sigma_n/\sigma_t)^{1/m} \quad [45]$$

the lowest value of σ_n is when $\tau = 0$:

$$\sigma_{n,min} = -a\sigma_t \quad [46]$$

At any point the gradient is given by:

$$\tan\psi_t = \frac{d\tau}{d\sigma_n} = \frac{c_0}{m\sigma_t}(a + \sigma_n/\sigma_t)^{(1-m)/m} \quad [47]$$

393 Referring to Fig. 11,

[48] $$s - \sigma_n = \tau \tan \psi_t = \frac{c_0^2}{m\sigma_t}(a + \sigma_n/\sigma_t)^{(2-m)/m}$$

[49] $$s = \sigma_n + \frac{c_0^2}{m\sigma_t}(a + \sigma_n/\sigma_t)^{(2-m)/m}$$

[50] $$\frac{ds}{d\sigma_n} = 1 + \frac{(2-m)c_0^2}{m^2\sigma_t^2}(a + \sigma_n/\sigma_t)^{(2-2m)/m}$$

394 This is always positive if $m < 2$ and indicates a switch of sign at:

[51] $$(a + \sigma_n/\sigma_t) = \left(\frac{(m-2)c_0^2}{m^2\sigma_t^2}\right)^{\frac{m}{2(m-1)}}$$

[52] $$\sigma_{n0} = \sigma_t \left(-a + \left(\frac{(m-2)c_0^2}{m^2\sigma_t^2}\right)^{\frac{m}{2(m-1)}}\right)$$

395 Which corresponds to a value of s at:

[53] $$s_0 = \sigma_{n0} + \frac{c_0^2}{m\sigma_t}\left(\frac{(m-2)c_0^2}{m^2\sigma_t^2}\right)^{\frac{2-m}{2(m-1)}}$$

396 It is thus necessary to work with Mohr's circles from $s = 0$ to s_0 that touch $\sigma_{n,min}$. Above s_0 the
397 circles are tangential to the yield surface (as shown in Fig. 11) and of radius t given as follows:

[54] $$t = \sqrt{\tau^2 + (s-\sigma)^2} = \tau\sqrt{1 + \tan^2\phi} = \tau \sec^2 \phi$$

398 For active conditions

[55] $$\sigma_v = s + t$$

[56] $$\sigma_h = s - t$$

399 For passive conditions

[57] $$\sigma_v = s - t$$

[58] $$\sigma_h = s + t$$

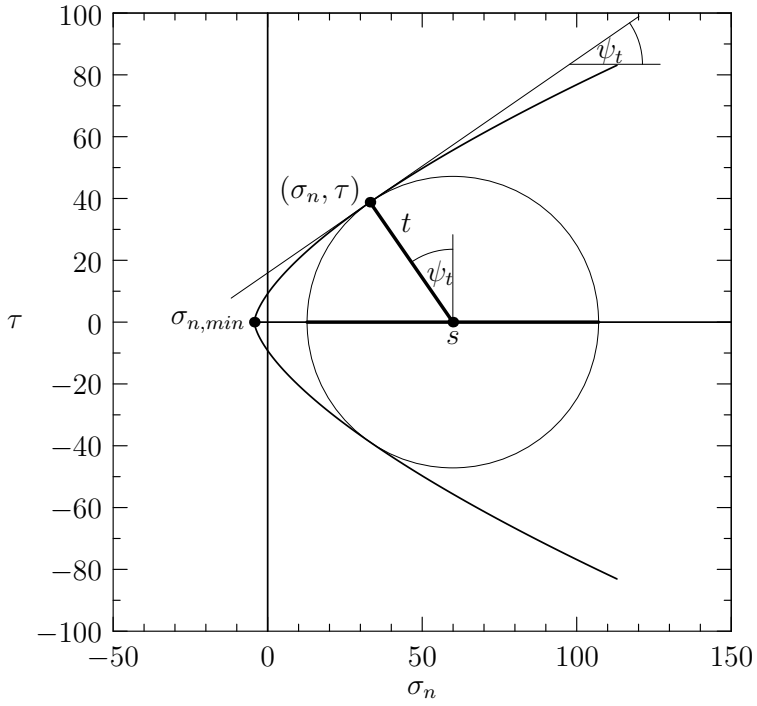

Fig. 11. Mohr's circle for non-linear yield surface, $c_0 = 5$, $a = 2.5$, $\sigma_t = 1.0/\tan(30)$, $m = 1.5$.